Astronomy & Astrophysics manuscript no. output
May 8, 2024

Magnetic Fields or Overstable Convective Modes in HR 7495:

Exploring the Underlying Causes of the Spike in the 'Hump & Spike' Features⋆

V. Antoci[1], M. Cantiello[2,3], V. Khalack[4], A. Henriksen[1], H. Saio[5], T. R. White[6], and L. Buchhave[1]

[1] DTU Space, Technical University of Denmark, Elektrovej 327, Kgs. Lyngby, 2800, Denmark
e-mail: antoci@space.dtu.dk
[2] Center for Computational Astrophysics, Flatiron Institute, 162 5th Avenue, New York, NY 10010, USA
[3] Department of Astrophysical Sciences, Princeton University, Princeton, NJ 08544, USA
[4] Département de Physique et d'Astronomie, Université de Moncton, Moncton, NB E1A 3E9, Canada
[5] Astronomical Institute, Graduate School of Science, Tohoku University, Sendai 980-8578, Japan
[6] Sydney Informatics Hub, Core Research Facilities, University of Sydney, NSW 2006, Australia

ABSTRACT

Context. More than 200 A and F type stars observed with Kepler exhibit a distinctive 'hump & spike' feature in their Fourier spectra. The hump is commonly interpreted as unresolved Rossby modes, while the spike has been linked to rotational modulation. This feature has led to the dubbing of these stars as 'hump & spike' stars. However, two competing interpretations exist for the spike.
Aims. This study aims to determine whether the observed spike in these stars is caused by magnetic phenomena, such as spots on the stellar surface, or by Overstable Convective (OsC) modes resonantly exciting low-frequency g modes within the star's envelope.
Methods. We analyzed photometric data from Kepler and TESS covering 4.5 years and four seasons, respectively, for HR 7495, the brightest 'hump spike' star with a visual magnitude of 5.06. Additionally, radial velocity measurements and spectropolarimetric data from three different epochs were incorporated to investigate magnetic fields and surface features. Furthermore, we computed a model-based artificial light curve examining the influence of OsC modes on phase-folded light curves.
Results. The analysis of phase-folded light curves indicates that the spike characteristics of HR 7495 align more closely with surface rotational modulation by stellar spots than with OsC modes. No significant magnetic fields were detected, which constrains the possible amplitude and geometry of the field. This is consistent with the hypothesis of a subsurface convective layer operating a dynamo, resulting in low-amplitude magnetic fields with potentially complex geometries. The observed variability patterns suggest the presence of multiple evolving spots, while the alignment of blue shifts with minimum flux seems to favour bright spots.
Conclusions. While the evolutionary stage of HR 7495 does not entirely preclude the possibility of OsC modes, the observational data overwhelmingly support the stellar spots hypothesis. Our analysis, combined with previous literature, suggests that at least the 'hump & spike' A and F type stars harbor an undetected weak magnetic field, likely driven by a dynamo mechanism.

Key words. stars – magnetic fields – rotational modulation

1. Introduction

Magnetic fields are among the most complex phenomena in astrophysics and are frequently invoked to reconcile discrepancies between theoretical models and observational data. They interact with atomic diffusion, turbulence, rotation, and notably influence the transport of angular momentum, critically impacting stellar evolution across various stages. Despite their acknowledged significance, our general understanding of magnetic fields including their strengths, geometrical configurations, origins, and even their very existence remains limited. In stars of masses below approximately 1.3 $M_\odot$, the presence of stellar magnetic fields is widely recognized (e.g., Donati & Landstreet 2009); however, for more massive A and F type stars on the main sequence, magnetic fields have been definitively measured in only about 10% of stars. Among these, a majority are chemically peculiar Ap stars with strong, well-organized magnetic fields of the order of kilogauss. Conversely, a minority exhibit weak magnetic fields, typically less than about 100 Gauss, as identified in several studies (Petit et al. 2011; Neiner et al. 2017; Zwintz et al. 2020; Blazère et al. 2016, 2020; Lignières et al. 2009; Neiner & Lampens 2015; Thomson-Paressant et al. 2023). From the theoretical standpoint, weak magnetic fields are predicted to potentially be ubiquitous in OBA stars, due to their rapid rotation and the presence of subsurface convective regions (Cantiello & Braithwaite 2011; Cantiello & Braithwaite 2019). Direct observation of weak fields, through spectropolarimetry, is feasible solely for very bright stars with relatively small values of $v \sin i$, suggesting the potential existence of numerous undetected weak magnetic fields in A and F stars. To address this detection challenge, indirect indicators of magnetic activity, such as stellar photospheric spots, have been employed. Thanks to missions like *Kepler* (Koch et al. 2010) and TESS (Ricker et al. 2015), detecting rotational modulation in hundreds of intermediate A and F type stars has become possible (e.g., Balona 2017; David-Uraz et al. 2019; Sikora et al. 2020; Trust et al. 2020; Henriksen et al. 2023a).

⋆ Based on observations made with the Nordic Optical Telescope, owned in collaboration by the University of Turku and Aarhus University, and operated jointly by Aarhus University, the University of Turku and the University of Oslo, representing Denmark, Finland and Norway, the University of Iceland and Stockholm University at the Observatorio del Roque de los Muchachos, La Palma, Spain, of the Instituto de Astrofisica de Canarias.

Observations of co-rotating stellar spots, which induce rotational modulation, are relatively straightforward when the signal-to-noise ratio is sufficient, as evidenced by light curves from the *Kepler* and TESS missions. However, elucidating the origins and causes of the aforementioned variability entails a more nuanced analysis. It is crucial to ascertain the presence of binary companions or potential contamination from nearby active stars, in addition to considering all plausible physical processes that could give rise to rotational modulation. Initial interpretations by Saio et al. (2018b) suggested that the distinct 'hump & spike' pattern observed in the Fourier spectra of certain stars results from unresolved Rossby modes (the hump), which are mechanically excited by deviated flows due to stellar spots at intermediate to high latitudes (the spike). Subsequently, Henriksen et al. (2023a,b) expanded on this work by identifying over 200 stars within the *Kepler* dataset that exhibit this specific pattern, further confirming the widespread occurrence and potential implications of these phenomena. However, Lee (2021); Lee & Saio (2020) proposed an alternate hypothesis for the spike, suggesting that overstable convective (OsC) modes present in rapidly rotating main-sequence stars could resonantly excite low-frequency g modes within the stellar envelope. In this scenario, the convective stellar core rotates marginally faster than its envelope, with the g modes manifesting an observable amplitudes at the photosphere causing the spike. In this case it would also be rotational modulation, but the spike would correspond to the rotational frequency of the convective core.

Henriksen et al. (2023a) performed an ensemble study on nearly 200 'hump and spike' stars, demonstrating that the spikes are more consistent with stellar spots generated by dynamo-driven magnetic fields. This is evidenced by their higher amplitudes in cooler and slightly evolved stars, aligning with theoretical predictions for dynamo activity that predicts stronger magnetic activity in stars with deeper convective envelopes (Cantiello & Braithwaite 2019). The spike lifetimes, not exceeding a few tens of days, align with expectations for the temporal behavior of magnetic features, while their occurrence shows no dependence on stellar mass, challenging theories that link spike frequencies with convective core rotation. This is because, in the case of OsC modes, the temporal variability of the spike would mirror the movement of convective cells inside the core, implying that the spike lifetimes would be on the convective turnover timescale. If that were the case, a correlation between spike lifetime and stellar mass should be present, which is not observed. Furthermore, harmonic analysis and phase-folded light curves revealed a non-sinusoidal pattern akin to what is expected from co-rotating stellar spots. Although magnetic field strength estimates reported by Henriksen et al. (2023a) were tentative, they aligned with the projections for non-Ap stars (Cantiello & Braithwaite 2011; Cantiello & Braithwaite 2019). Notably, the identification of stars potentially in a post-main-sequence phase argues against overstable convective modes due to the absence of a convective core, albeit the evolutionary phase needs to be determined from more detailed modeling. This body of evidence, complemented by recent spectropolarimetric observations of stars like β Cas (Zwintz et al. 2020), supports the hypothesis that intermediate-mass stars can harbor dynamo-generated magnetic fields. However, detailed analysis of individual single stars are required to arrive to a clear conclusion.

In this article, we present in-depth analyses of the brightest 'hump and spike' star, HR 7495 (V=5.06), observed photometrically from space with *Kepler* and TESS. We further collected spectroscopic data with FIES at the NOT (Nordic Optical Telescope), and performed spectropolarimetric observations with ESPaDOnS at the Canada-France-Hawaii Telescope (CFHT)[1]. We compare contemporary radial velocity and flux measurements, analyze the shape of the phase-folded light curves, and discuss the temporal behavior in the context of stellar spots and OsC modes. We further discuss the evolutionary stage of HR 7495 and estimate the spot size/contrast based on the non-detection of a magnetic field.

2. Data

This section details the datasets analyzed to identify the spike's origin in HR 7495. We outline the sources and methodology behind our data collection.

2.1. Photometry

HR 7495 (V=5.06, HD 186155, KIC 9163520, TIC 271545295, RA 19h 40m 50.18s; Dec +45° 31' 29.8") is a luminous F5 II-III spectral type star within the *Kepler* field. Utilizing data from Gaia DR3 (Gaia Collaboration et al. 2022) alongside the GSP-Phot and FLAMES modules, we have extracted the parameters listed in Table 1. The GSP-Phot module (General Stellar Parametrizer from Photometry) employs low-resolution spectra from the BP/RP instruments to calculate the effective temperature, while the FLAMES module ascertains luminosity, mass, and age, leveraging parallaxes, GSP-Phot inputs, and an extinction map from DR2 photometry (Lallement et al. 2019). Notably, the temperature uncertainty derived from GSP-Phot is considered to be underestimated. Consequently, we have adopted an error margin of approximately 110 K, as recommended by Duerfeldt et al. 2024 (submitted).

Table 1. Astrophysical Parameters of HR 7495. The spike parameters are based on *Kepler* data.

Stellar Parameter	Value
Parallax [mas]	19.75 ± 0.07
Luminosity [$L_\odot$]	$18.49^{+0.13}_{-0.12}$
$T_{\rm eff}$ [K]	6610±110
Radius [$R_\odot$]	3.30± 0.07
Spike frequency* [cd^{-1}]	0.6770 ± 0.0005
Spike period* [d]	1.4471 ± 0.0011
Spike Amplitude* [ppm]	173.3 ± 0.8
Spike lifetime* [d]	19 ± 0.1
$v \sin i$* [kms^{-1}]	41 ± 4
inclination i* [deg]	21 ± 2
rotational velocity $v_{\rm rot}$* [kms^{-1}]	113 ± 2

*Values from Henriksen et al. (2023a).

Due to its brightness, HR7495 was not directly observed with *Kepler*. However, using the *Kepler* Smear Campaign (Pope et al. 2019), long-cadence data were extracted from the entire mission, with only Quarter 0 missing. The length of the data set is 1458.5 days (Table2). In the *Kepler* Smear Campaign, Pope et al. (2019) utilized a method to construct light curves for stars that were otherwise too bright to be directly observed by the *Kepler* telescope due to saturation. Because the *Kepler* camera does not have a

[1] The Canada-France-Hawaii Telescope (CFHT) is operated by the National Research Council of Canada, the Institut National des Sciences de l'Univers of the Centre National de la Recherche Scientifique of France, and the University of Hawaii. The operations at the Canada-France-Hawaii Telescope are conducted with care and respect from the summit of Maunakea which is a significant cultural and historic site.

shutter, light continued to fall on the CCD during read-out, resulting in a smearing of the image as the charges in each pixel were shuffled along columns. To correct for this smear, 'masked' and 'virtual' rows on either side of the science pixels measured the amount of light that fell on each column during read-out so that it could be subtracted. The saved 'collateral' smear data could then be used to perform photometry on bright stars that dominated the flux in their columns (Kolodziejczak & Caldwell 2011; Pope et al. 2016), as was the case with HR 7495.

The TESS data analysed in this work are the 2-min Presearch Data Conditioning SAP (PDCSAP) light curves provided by the TESS Science Team, which are publicly available from the Mikulski Archive for Space Telescopes (MAST[2]). The PDCSAP are Simple Aperture Photometry (SAP) data from which long term trends have been removed using so-called Co-trending Basis Vectors (CBVs). PDCSAP data are usually cleaner than the SAP flux and will have fewer systematic trends, which is important when looking a periods of the order of days.

2.2. Spectroscopy

We acquired contemporaneous stellar spectra alongside TESS observations using the Fiber-fed Echelle Spectrograph (FIES; Telting et al. (2014)) at the Nordic Optical Telescope (NOT; Djupvik & Andersen (2010)) located at the Roque de los Muchachos Observatory in La Palma, Spain. We used the higher resolution fibre with R = 67000 and exposed HR 7495 for 80 sec. The reduction of the FIES spectra followed the methodology outlined by Buchhave et al. (2010), involving bias subtraction, flat fielding, order tracing and extraction, and wavelength calibration. The latter utilized ThAr spectra obtained immediately before or after each scientific exposure to ensure accuracy. Radial velocities (RVs) were determined through multi-order cross-correlation (Buchhave et al. 2010), employing the spectrum with the highest SNR as a reference template (BJD=2459772.5348040, see Table A.1).

2.3. Spectropolarimetry

HR7495 was observed with the spectropolarimeter ESPaDOnS (Echelle SpectroPolarimetric Device for Observations of Stars) at the Canada-France-Hawaii Telescope (CFHT) in July and October of 2023 (see Table3). The first and second columns in Table 3 present, respectively, the Heliocentric Julian Date of the observations and the measured mean longitudinal magnetic field ($\langle B_z \rangle$) with the corresponding error bars. The exposure time and the signal-to-noise ratio (SNR at echelle order 34) of the obtained Stokes I & V spectra are shown in the third and fourth columns, respectively.

Employing the deep-depletion e2v device Olapa, the spectropolarimeter ESPaDOnS has acquired high-resolution (R=65,000) Stokes I & V spectra of HR 7495 in the spectral domain from 3700Å to 10000Å with SNR≥800. The optical characteristics of the spectrograph as well as the instrument performances are described in detail by Donati et al. (2006)[3]. The dedicated software package Libre-ESpRIT (Donati et al. 1997) has been employed to reduce the non-polarized Stokes I spectra and the circular polarisation Stokes V spectra. Individual normalization was applied to all the spectra to optimize the final SNR.

[2] https://mast.stsci.edu/portal/Mashup/Clients/Mast/Portal.html

[3] For more details about this instrument, the reader is invited to visit www.cfht.hawaii.edu/Instruments/Spectroscopy/Espadons/

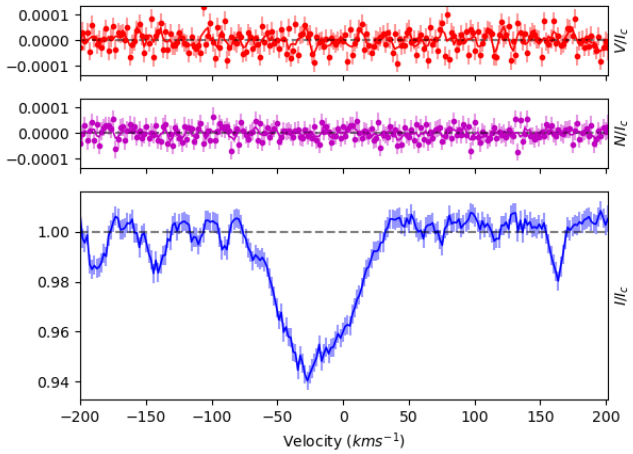

Fig. 1. Averaged LSD-profiles in Stokes V (top panel) and I (bottom panel) obtained for HR 7495 (spectrum with HJD=2460136.10812) using a mask of 7000 lines. The middle panel presents the N (noise) LSD-profile that shows a stochastic noise similar to the one found in the average Stokes V LSD-profile.

The Least-Squares Deconvolution (LSD) technique, as implemented by Colin Folsom (Folsom 2024) in Python[4] , was employed to probe the mean longitudinal magnetic field. Our target was observed across three distinct epochs (see Table 2 for details). Analysis of the first spectrum (HJD=2460136.10812) having high signal to noise ratio (reaching 820 in Stokes I and 790 in Stokes V spectra at the order #34 with the central wavelength λ666 nm, see Table 3) has not resulted in a detection of a statistically significant $\langle B_z \rangle$. To enhance SNR and reduce error margins for subsequent HR7495 observations at varied rotational phases (see SNR in Table 2), we collected four consecutive spectra, each comprising four polarization scans, striving for the highest SNR within a practical total accumulation time. Unfortunately, none of the observations yielded a statistically significant magnetic field detection in HR 7495 (see, for example, Fig. 1). Even when combining two spectra with the largest fields, we obtained only $\langle B_z \rangle = -4 \pm 2$ G, indicating no significant magnetic field presence at the observed epochs. For the LSD analysis, we used a mask created by John Landstreet, tailored for $T_{\rm eff}$ =6750 K and solar metallicity, closely matching the characteristics of HR 7495, and encompassing over 7000 lines. The inspection of the LSD Stokes V profile revealed no discernible signal (see Fig. 1), supporting the absence of a significant magnetic field.

It is important to note that the observational scheduling did not allow for the selection of specific rotational phases optimal for magnetic field detection. Ideally, observations should coincide with peak visibility of the stellar spot associated with a dynamo action. However, given the low amplitude of the rotational modulation observed, strong magnetic fields were not anticipated. In addition, the complexity of the dynamo-driven magnetic field configurations could also lead to cancellation effects, thus potentially explaining non-detection of the statistically significant $\langle B_z \rangle$. For conclusive results, additional observations aimed at systematically sampling the rotational phase should be performed.

[4] https://github.com/folsomcp/specpolFlow, https://github.com/folsomcp/LSDpy

Table 2. Data

Telescope	Method	Time Span [days]	Quarters/sectors
Kepler	Photometry	1459.5	17 (Q0 missing)
TESS 2019	Photometry	54	14, 15
TESS 2021	Photometry	54	40, 41
TESS 2022	Photometry	27	55
TESS 2024	Photometry	54	75, 76
FIES	RV	10 epochs (30 measurements)	
CFHT	Spec.Pol.	3 epochs (9 measurements)	

Table 3. Summary of spectropolarimetric observations of HR 7495 with ESPaDOnS.

HJD	$\langle B_z \rangle \pm \sigma_B$ [G]	t_{exp} [sec]	SNR Stokes I/V
2460136.10812	1.2 ± 2.8	250	820/790
2460238.84517	0.3 ± 5.2	252	860/800
2460238.84919	-2.0 ± 3.5	252	850/790
2460238.85322	-2.5 ± 3.5	252	850/800
2460238.85725	-0.7 ± 2.8	252	860/810
2460243.71444	-1.3 ± 2.8	252	860/810
2460243.71846	-6.2 ± 2.9	252	850/810
2460243.72247	-3.0 ± 3.1	252	850/810
2460243.72649	-0.8 ± 2.8	252	850/790

3. Data analyses

The *Kepler* mission provided near-continuous observation of HR 7495 for over four years, in contrast to TESS, which collected data in intervals of 27 or 54 days, separated by gaps of 1-2 years (see Table 2 for details). Consequently, we opted to analyze each TESS dataset independently. Using the same analysis methods as Henriksen et al. (2023a), we determine the spike amplitude and frequency across different TESS observations as follows: for TESS 2019, a spike amplitude of 66 ± 6 ppm and frequency of 0.677 ± 0.016 cd^{-1}; for TESS 2021, a spike amplitude of 132 ± 5 ppm and frequency of 0.677 ± 0.009 cd^{-1}; for TESS 2022, a spike amplitude of 152 ± 9 ppm and frequency of 0.676 ± 0.020 cd^{-1}; and for TESS 2024 , a spike amplitude of 107 ± 8 ppm and frequency of 0.6769 ± 0.01 cd^{-1}. These results are in agreement with the spike frequency of 0.6770 ± 0.0005 cd^{-1} derived from *Kepler* data (see also Table 1), which will be used for all our analyses. In Fig. 2 we show all the photometric data phased-folded with the spike frequency mentioned.

To visualise and interpret the rotational modulation signal, i.e., the spike, we utilized a bandpass filter employing Weighted Least Squares (see Rasmus Handberg's Github[5] repository for details). Our focus was narrowed to signals within the frequency range between 0.672 and 5 cd^{-1}, choosing the lower limit specifically to omit the hump component but keep the harmonics, as they are either due to the non-sinusoidal shape of the light curve or due to OsC modes of higher azimuthal order. Figure 3 displays the Fourier spectra of all our photometric datasets, with the expected hump region shaded in gray. Due to its relatively low amplitude, the hump is primarily discernible in the *Kepler* data. Further, we display the original (unfiltered) data in blue and the bandpass-filtered data in orange. Dashed vertical lines mark the identified spike frequency alongside its first and second harmonics. It is important to acknowledge that the TESS data resolution falls short of completely separating the hump from the spike signal. Nevertheless, the comprehensive 17 quarters of *Kepler* observations have enabled us to establish distinct frequency boundaries with great precision.

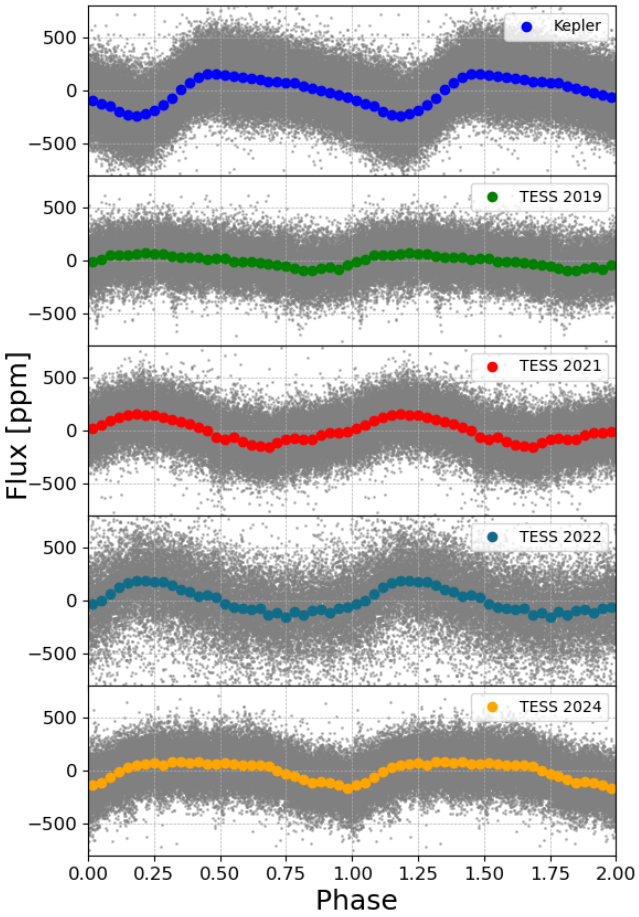

Fig. 2. Phase-folded original *Kepler* and TESS data displayed in gray, using the spike frequency derived from *Kepler* data. Colored curves represent the binned data, showing the median value in each of the 80 arbitrarily chosen bins.

We investigate the temporal variability of the spike by phase-folding the observed time series around a spike frequency of 0.6770 d^{-1}. To ensure consistency across datasets, we aligned all observations to a reference epoch of 2459797.10309 (T0 of the TESS 2022 dataset), facilitating the comparison of contemporaneous TESS and RV data, as discussed in Section 6.

[5] https://github.com/rhandberg/timeseries/tree/master

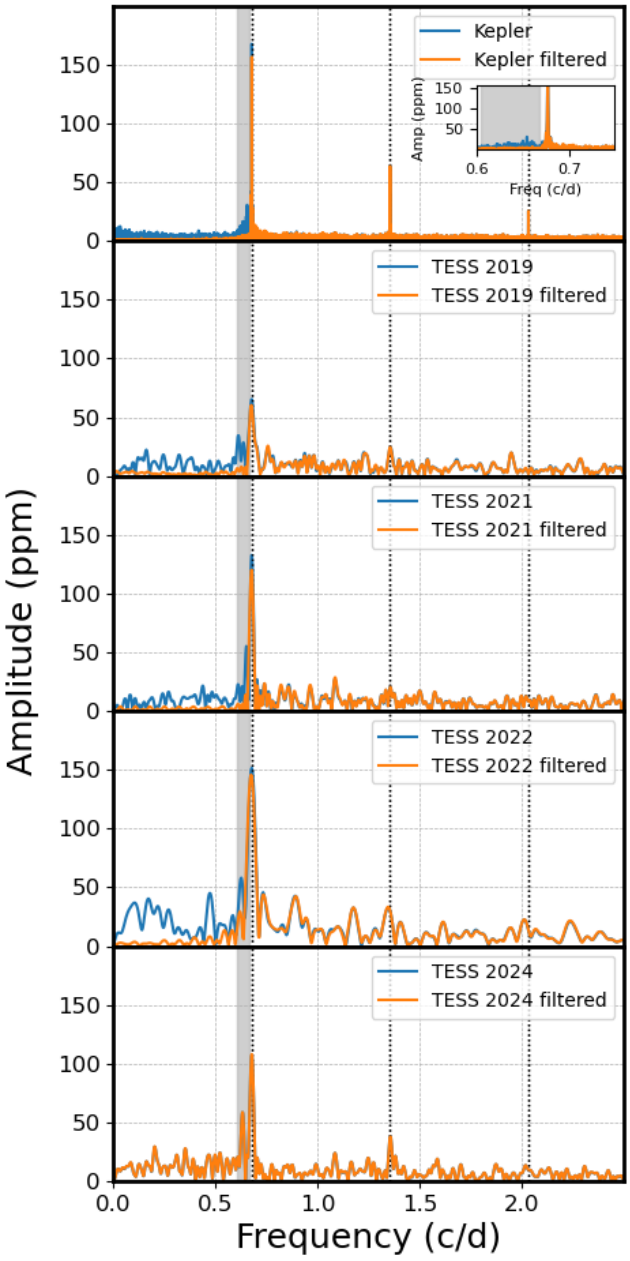

Fig. 3. Fourier spectra of *Kepler* and TESS data, with *Kepler* shown in the upper panel and TESS data in panels 2 to 5. Original unfiltered data are depicted in blue, while band-pass filtered data are shown in orange. The gray area highlights the position of the hump, and dotted black vertical lines mark the spike frequency and its harmonics.

To analyse the temporal behaviour of the light curve, we grouped the each photometric data set into subsets corresponding to three rotation phases and divided these into 30 equal phase bins, averaging the data within each bin containing roughly 35 data points. Three rotation phases correspond to a span of 4.35 days, roughly a quarter of the spot lifetime inferred from *Kepler* data (see Table 1). This approach allows for a detailed examination of the temporal spike variability and the potential tracking of spot evolution. Figures 4 and 5 display the original and bandpass-filtered data from the TESS 2022 dataset, respectively. These figures illustrate how bandpass filtering reduces scatter in the binned data, thereby enhancing our ability to interpret the signal attributed to the spike. Observational gaps exceeding twice the rotation period were identified in both the *Kepler* and TESS datasets. We tailored our analysis to include only the data preceding these gaps, thereby excluding any subsequent data. This approach ensures our focus remains on continuous data sequences, effectively preventing potential distortions that could arise from analyzing extensive intervals devoid of data. Figure 6 shows four different parts of the *Kepler* data after bandpass-filtering, which are well distributed over the entire *Kepler* observing period. We discuss the variability further in Section 6.

4. Theoretical expectations for stellar spots

Here we look at the possible change in stellar luminosity induced by the presence of surface magnetic fields. Stable, large scale magnetic fields in thermal equilibrium are expected to lead to very small perturbations to the stellar luminosity. Fuller & Mathis (2023) predict that even for the strongest observed fields in main sequence stars ($\sim$ 10 kG), the bolometric luminosity variation is $\delta L/L \leq 10^{-6}$, which at present is not detectable even with high-quality space-based photometry.

The influence of magnetic fields on systems outside of thermal equilibrium can significantly differ. In stars exhibiting transient magnetic phenomena such as magnetic spots due to dynamo action, the lifespan of these magnetic spots may be substantially shorter than the local thermal timescale of the star, depending on how deep the spots are. In stars with convective envelopes transporting a large fraction of the stellar flux, such magnetic fields can temporarily interrupt the transport of convective energy, which explains why on the Sun magnetic spots appear dark: they are not in thermal equilibrium with the layers below them. In stars with radiative envelopes the expectation is that magnetic spots should be bright, due to the local decrease of total pressure they induce (Cantiello & Braithwaite 2011; Cantiello & Braithwaite 2019). Predictions for the bolometric fluctuations produced by such magnetic spots depend on their size and the field amplitude. However such predictions do not consider the effect of thermal diffusion, which might significantly mitigate the flux perturbations, particularly for spots that persist longer than the local thermal timescale (Fuller & Mathis 2023).

We follow Cantiello & Braithwaite (2011) to calculate the bolometric luminosity perturbation induced by a spot at the surface of stars with envelopes dominated by radiative energy transport, keeping in mind values recovered using this theory likely correspond to upper limits. Similarly to Henriksen et al. (2023a), we write the luminosity perturbation as:

$$\frac{\Delta L}{L} \simeq \frac{4\Delta T}{T} = \frac{4\nabla_{\rm rad}}{\beta}. \quad (1)$$

with

$$\beta = \frac{P_{\rm tot}}{P_{\rm mag}} = \frac{P_{\rm tot}}{B^2/8\pi},$$

where $P_{\rm mag}$ is the component of the pressure due to the presence of the magnetic field, $P_{\rm tot}$ is the total pressure and B the magnetic field strength. This equation provides the luminosity contrast of a magnetic spot compared to the unperturbed stellar luminosity. In order to compare to observations, one has to account for the relative size of the spot compared to the stellar radius. To do so

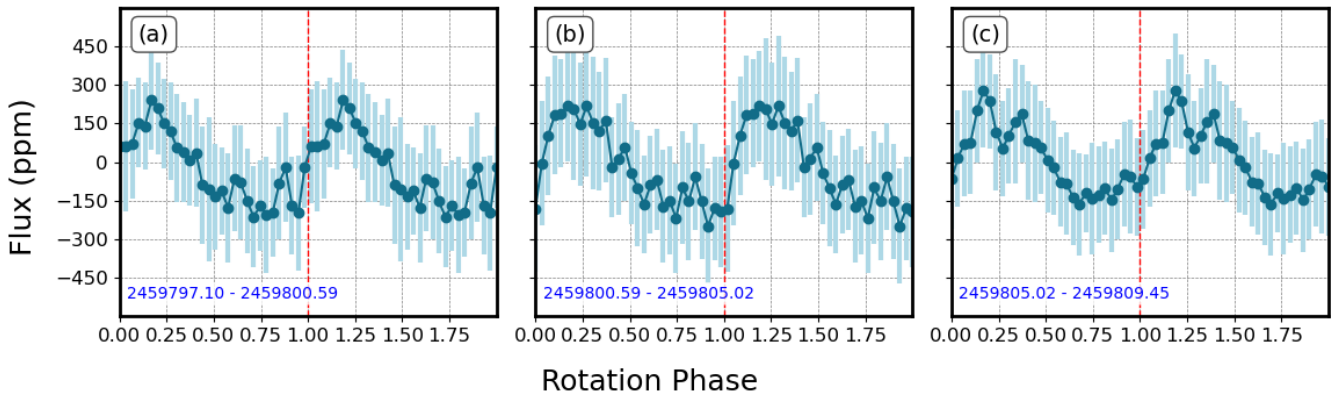

Fig. 4. Phase-folded original data. Each panel presents three rotation periods combined and binned into 30 equal segments. The petrol-blue data points are the binned the bars representing the standard deviation in each panel.

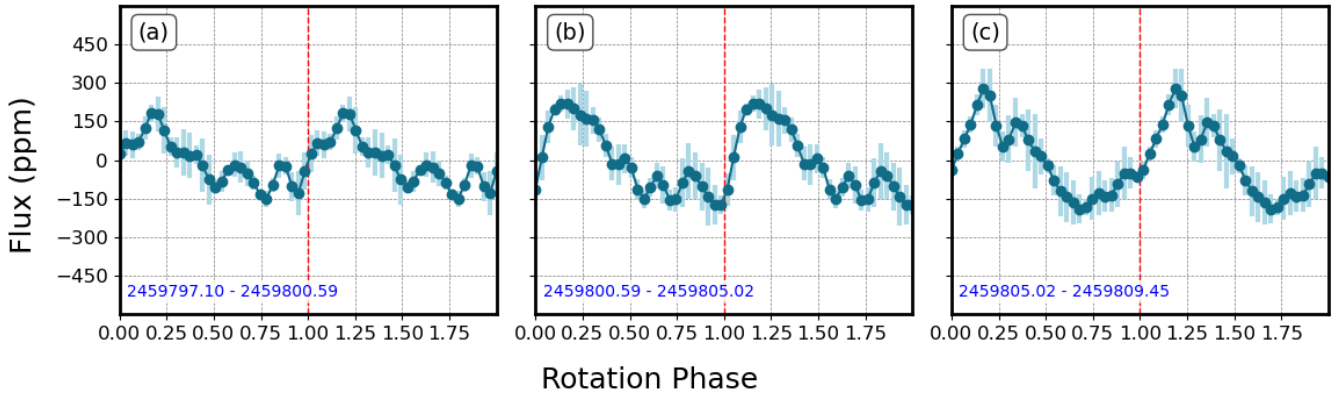

Fig. 5. Phase-folded band-passed data. Each panel presents three rotation periods combined and binned into 30 equal segments.The petrol-blue data points are the binned the bars representing the standard deviation in each panel.

we add the filling factor $f = (r/R)^2$, where r is the radius of the spot and R is the stellar radius.

$$\frac{\Delta L}{L} = \frac{4\nabla_{\rm rad}}{\beta}\left(\frac{r}{R}\right)^2. \quad (2)$$

It is important to recognize the interplay between the size of the spot and its temperature (or luminosity) contrast: A large spot with minimal luminosity contrast can result in a brightness change similar to that of a smaller spot with a greater luminosity contrast. Using the definition of β, equation 2 can be written as:

$$\frac{\Delta L}{L} = \frac{4\nabla_{\rm rad}B^2}{8\pi P_{\rm tot}}\left(\frac{r}{R}\right)^2 \quad (3)$$

We can then replace the ratio $\Delta L/L$ with the observed photometric amplitude ($A_{\rm spike}$) in the *Kepler* and TESS data. Note that our calculation assumes a single spot and we do not correct for the instrument bandpass.

Since we have limits on the observed magnetic field amplitude, we can then calculate the minimum size of a single magnetic spot able to induce the observer luminosity variation:

$$f \simeq \frac{A_{\rm spike}}{B^2}\frac{2\pi P_{\rm tot}}{\nabla_{\rm rad}} \quad (4)$$

Using the stellar models described in Henriksen et al. (2023a) we recover values of $\nabla_{\rm rad}$ and $P_{\rm tot}$ suitable for HR 7495 ($\nabla_{\rm rad} \approx 0.13$ and $P_{\rm tot} \approx 8 \times 10^3$). Plugging in 15 G as upper limit for the magnetic field (see table 3) and 100 ppm as typical spike amplitude, this implies a minimum filling factor $f \approx 0.17$, or a spot minimum radius $r \approx 0.42\,R$.

We want to emphasize that this is a very simplified treatment, intended only to demonstrate that it is possible to explain the periodic changes in luminosity of HR 7495 with a magnetic spot that eludes spectropolarimetric detection. For instance, Figures 5, 6, and 10 suggest that several magnetic spots may be present on the surface of HR 7495, complicating the interpretation of the light curve and the derivation of the filling factor. This complexity also makes the adopted limit on the maximum magnetic field associated with surface spots uncertain, as spectropolarimetric detection is likely influenced by cancellation effects.

5. Theoretical expectation of the phase-folded light curve

In the context of OsC modes, the three peaks observed in the Fourier transforms in Fig. 3 correspond to prograde sectoral g modes with azimuthal orders of $m = 1, 2, 3$. We adopt the convention that $m > 0$ indicates prograde modes. If the convective

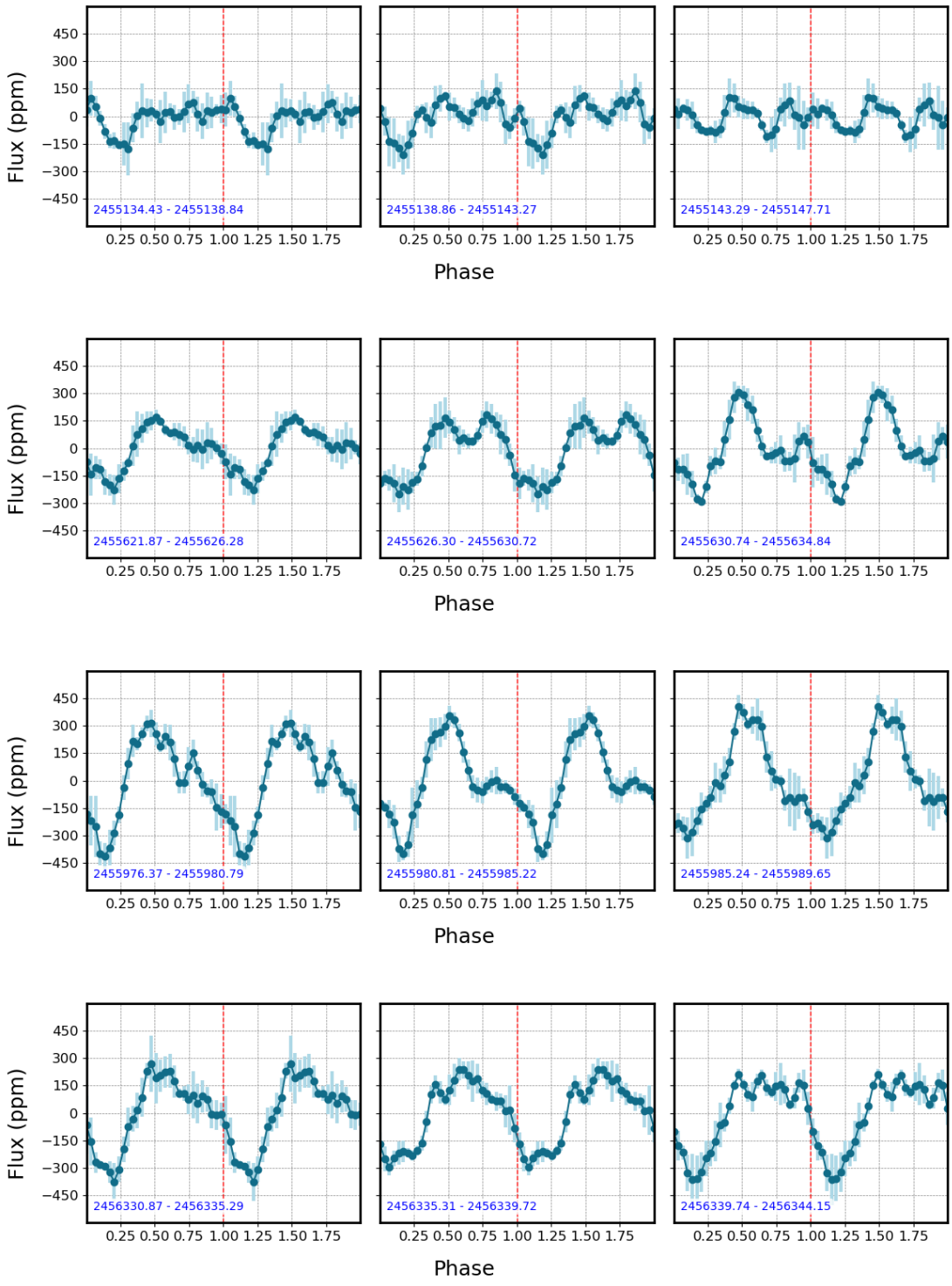

Fig. 6. *Kepler* data, selected subsets. Each panel presents data combined over three rotation periods and binned into 30 equal segments. The data in a given row are consecutive. The petrol-blue data points represent the binned data, with the bars indicating the standard deviation in each panel.

core rotates slightly faster than the envelope, high radial order g modes could be resonantly excited by the OsC modes in the convective core (Lee & Saio 2020; Lee 2021). Writing the rotation rates of the core and envelope as $\nu_{\rm rot}^{\rm co}$ and $\nu_{\rm rot}^{\rm en}$, respectively, we have a relation

$$\Delta\nu_{\rm rot} \equiv \nu_{\rm rot}^{\rm co} - \nu_{\rm rot}^{\rm en} \ll \nu_{\rm rot}^{\rm co}\,,\nu_{\rm rot}^{\rm en}.$$

As the envelope (rotating at $\nu_{\rm rot}^{\rm en}$) experiences OsC frequencies of $m\Delta\nu_{\rm rot}$, high radial order g modes are expected to be resonantly excited with frequencies, $\nu_{\rm cor}^{m} \sim m\Delta\nu_{\rm rot}$. In the inertial frame, these g modes have frequencies of

$$\nu_{\rm int}^{m} = \nu_{\rm cor}^{m} + m\nu_{\rm rot}^{\rm en} \approx m\nu_{\rm rot}^{\rm en}$$

Thus, these prograde g modes with $m = 1, 2, 3$ can be identified with the three spikes seen in the Fourier diagram for the *Kepler* data in Figure 3.

Based on the above models for the three spikes in the *Kepler* Fourier diagram for HR 7495, we have constructed expected light variations as function of rotation phase, which are shown in Figure 7. The frequency of a resonantly coupled g mode, $\nu_{\rm cor}$, in the co-rotating frame of the envelope is much smaller than the envelope rotation frequency $\nu^{\rm en}_{\rm rot}$, so that the spin parameter of the mode is very high $2\nu^{\rm en}_{\rm rot}/\nu_{\rm cor} \gg 1$. Among the g modes with high spin parameters, only prograde sectoral modes are visible having broadly distributed amplitudes on the surface, symmetric to the equator, while the other g modes are confined into a narrow zone around the equator and anti-symmetric to the equator (see e.g. Appendix in Saio et al. 2018a). For this reason, we have obtained light curve in Figure 7 by superposing the prograde sectoral g modes of $m = 1, 2, 3$ with amplitude ratios of $1 : 0.37 : 0.14$ that are consistent with the amplitudes in the *Kepler* Fourier diagram shown in Figure 3 (top panel).

Using the traditional approximation of rotation (e.g., Lee & Saio 1997; Townsend 2003), we have derived the latitudinal dependence of the eigenfunction from the Hough function. While the Hough function is dependent on the spin parameter, it becomes nearly independent for prograde sectoral modes when the spin parameter is sufficiently large. We assumed a high spin parameter of $30/m$ for each g mode with azimuthal order m. Additionally, assuming a limb-darkening parameter of $\mu = 0.6$ and an inclination of the line-of-sight to the rotation axis, we integrated the local flux perturbation (assumed to be proportional to the temperature perturbation) on the visual surface at each pulsation phase.

In Figure 7 we have adopted an inclination angle of 20°, while the results are insensitive to the angle because the amplitudes of prograde g modes are broadly distributed in latitude. Some bumps are seen in the light curve in this figure, which come from the contributions from $m = 2$ and 3 modes. The bump locations depend on the phase relations among of $m = 1, 2, 3$ modes. In Figure 7 we show the effects of phase shifts of $m = 3$ mode. The black solid line show the case in which no initial phase shift is imposed, while red and blue dashed lines show the cases where phase shifts of $\pi/4$ and $\pi/2$ are, respectively, imposed for the $m = 3$ mode. As expected, bumps in the light curve are somewhat affected by these phase shifts. The frequencies of the three modes in the co-rotating frame differ, though very little. For this reason we expect that small differences $|\nu^{\rm m}_{cor} - \nu^{\rm m'}_{cor}|$ would slowly modify the phase relations among the g modes to result in gradual variations in the light curves, which could correspond to the observed gradual variations in folded light curves.

To evaluate this model, we subdivided the light curve into subsets of 150 days to assess the stability of the phases for all three peaks. To maintain a sufficiently high signal-to-noise ratio, we refrained from using smaller subsets. Using Period04 (Lenz & Breger 2014), we conducted least-squares fitting, with the frequencies held fixed while allowing the amplitudes and phases of all three peaks to vary. The results, illustrated in Fig. 8, reveal that although the phase differences between the spike (F1) and the first harmonic (F2), and between the spike and the second harmonic (F3), start around $\pi/2$ in the initial subsets, they stabilize to less than $\pi/4$ for the majority of the data. Simultaneously, significant amplitude variability was observed throughout the dataset, with the second harmonic peak (m=3, if OsC modes) vanishing in the final two subsets.

This variability, primarily manifesting as amplitude changes rather than phase shifts, aligns with observations from the phase-folded light curve in Fig. 6. Moreover, the minimum flux consistently occurs between phase 0 and 0.2, as depicted throughout the Kepler observations in Fig. 6. Notably, during periods of the most significant phase change—when analyzing the data in shorter segments, the first harmonic (F2) exhibits a higher amplitude than the spike frequency, which contradicts expectations for OsC modes (see Section 6 and Fig. 9 for more details).

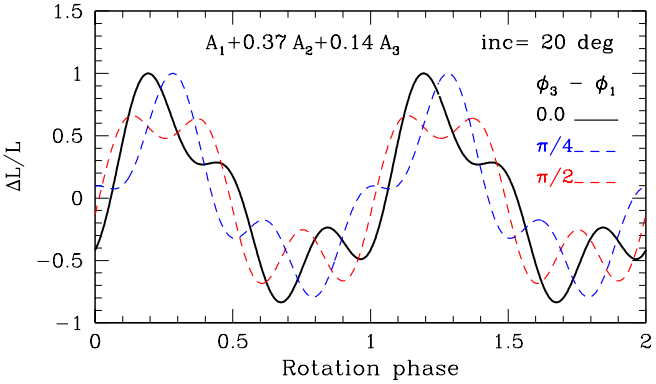

Fig. 7. Light curves expected if the sectoral prograde g modes of $m = 1, 2, 3$ are superposed, in which amplitude ratios of each mode are given as $1 : 0.37 : 0.14$, consistent with the amplitudes in the *Kepler* Fourier diagram (Fig. 3; top panel). For black solid line the initial phases of all modes is set to be identical. Since the the initial phases of these modes are arbitrary, we examined the effect of phase shift of $m = 3$ mode as indicated in the lower panel. The initial phase of the $m = 2$ mode is set equal to that of $m = 1$mode.

The generally stable phases in over half of the dataset imply that if OsC modes were present, we would expect to see light curve variations similar to the black or blue curves, with harmonic phase shifts of less than $\pi/4$, as shown in Fig. 7. However, the discrepancies observed in Fig. 6 lead us to conclude that the OsC model does not adequately explain the temporal variability of the *Kepler* phase-folded light curves.

6. Results and Discussion

The aim of this work is to distinguish between two scenarios: (1) rotational modulation induced by co-rotating spots driven by magnetic fields, or (2) OsC modes in the convective core resonantly exciting g-modes that reach the surface. Henriksen et al. (2023a) performed ensemble analyses of all *Kepler* hump and spike stars, and concluded that scenario (1) is more likely, however, scenario (2) could not be excluded. HR 7495 is the best target to follow-up and perform in depth analyses.

In the context of spots, observing clear photometric variations in a star viewed at a low inclination of $\approx$ 20°, implies that the spots causing these variations are not circumpolar. The observed flux changes (see, Fig. 5 and Fig. 6) indicate that the spots must reside at lower latitudes, allowing them to rotate into and out of view despite the pole-oriented perspective. The phase-folded data depicted in Fig. 5 and Fig. 6, clearly show evolving features that could be consistent with spots moving and merging. In the case of the *Kepler* data, it is noteworthy that the minimum in flux observed between phase 0 and 0.25 appears stable for almost 4.5 years when visible. Additionally, the data suggest that HR 7495 exhibited increased activity in the second half of the mission (see amplitude increase in the upper panel of Fig. 8), consistent with a dynamo that could display cycles similar to those observed in other stars (e.g., Jeffers et al. 2023).

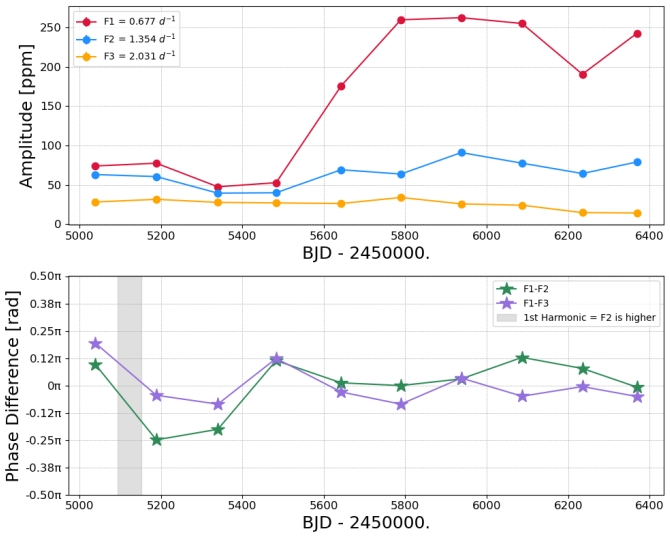

Fig. 8. Upper panel: Amplitudes determined for subsets of the *Kepler* data spanning 150 days. The BJD corresponds to the averaged value for each data bin. Uncertainties are smaller than the symbols depicted. Lower Panel: Phase differences are shown with the average difference removed to enhance readability. The gray area highlights parts of the dataset where the 1st harmonic exhibits a higher amplitude than the spike, as illustrated in Fig.9.

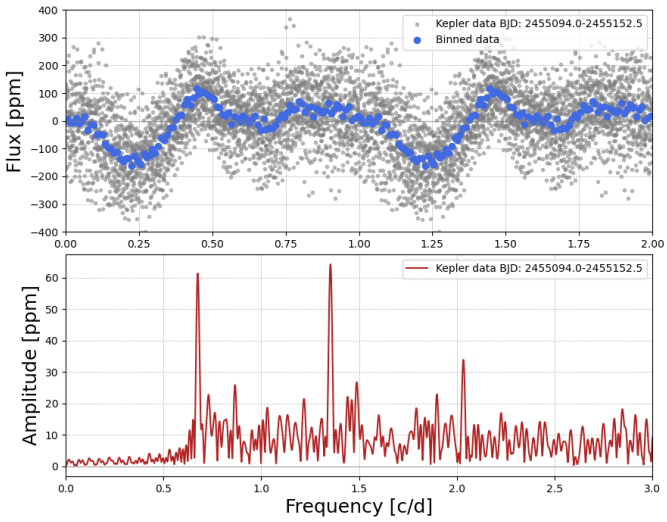

Fig. 9. Upper Panel: Phase-folded, band-pass-filtered *Kepler* data from the start of the observation period (dates detailed in the legend). Lower Panel: Fourier transform of the light curve for the corresponding time-frame. Note the pronounced amplitude of the first harmonic (twice the fundamental spike frequency), suggesting the presence of stellar spots.

In the case of stellar spots, spike harmonics in the Fourier spectrum arise due to the non-sinusoidal shape of the light curve. However, for OsC modes, the harmonics represent modes with different azimuthal orders as mentioned above, and their amplitudes are expected to decrease monotonically due to geometrical effects. Henriksen et al. (2023a) demonstrated that 36 out of 162 stars, when analyzing the entire *Kepler* dataset, exhibit harmonics consistent with the interpretation of stellar spots. In the case of HR 7495, as shown in Fig. 3, none of the spike harmonics exceed the spike amplitude. However, analyzing the *Kepler* dataset in segments allowed us to determine that the amplitude of the first harmonic can be higher than that of the spike amplitude, as depicted in Fig. 9. This subset of data indicates that the spike in HR 7495 is consistent with the presence of stellar spots, confirming the spike frequency as the surface rotation frequency.

We obtained contemporaneous TESS and RV data, as well as magnetic field measurements, which are displayed in Fig. 10. The upper panel shows the phase-folded, bandpassed TESS 2022 data set, while the lower panel presents the RV phase-folded curve. The yellow vertical lines represent the phases at which we observed HR 7495 spectropolarimetrically. Generally speaking, for a star with a single dark spot, viewed equator-on, photometric variations would appear as periodic dips in brightness when the spot rotates into view, with the depth depending on the spot's size and contrast. Radial velocity variations would exhibit a sinusoidal pattern during the half of the rotational phase when the spot is visible, showing redshifts as the spot approaches and blue shifts as it recedes. No RV variability would be observed when the spot is on the far side of the star, out of view. The inclination angle of the star's rotational axis to our line of sight plays a crucial role; these variations are most pronounced when viewing the star equator-on and diminish as the inclination angle decreases, altering the detectability and amplitude of both photometric and RV signals.

Figure 10 reveals the presence of multiple spots on HR7495, a finding supported by Figure 6. The maximum blue shift aligns closely with the minimum flux, with both the flux and RV curves displaying non-sinusoidal shapes. The distinct non-sinusoidal nature of the RV curve in HR7495 cannot be explained by the presence of g-modes alone, unless there is considerable contribution from m=2 and m=3 modes. The alignment of the blue shift with minimum flux may indicate that the spots are bright. Interestingly, similar behavior was observed in HD 188774 (Lampens et al. 2013), where the authors noted the maximum blue shift at minimum flux. Unlike HR 7495, HD 188774 displays a double-wave pattern, which suggests the presence of two opposing spots. It is important to note that HD 188774 indeed possesses a magnetic field below 100G, as detected by Neiner & Lampens (2015). Our observations of anomalously large RV amplitudes in HR 7495 echo the findings of Lampens et al. (2013), who noted disproportionately large RV amplitudes compared to flux in HD188774. We speculate that Rossby modes may be contributing to the enhancement of these RV amplitudes. While a detailed study exploring how magnetic fields and Rossby modes interact would yield further insights, such an analysis is beyond the scope of this paper.

6.1. Evolutionary stage of HR 7495

Another aspect that can help distinguish between the two scenarios is the evolutionary stage of HR 7495. OsC modes can only be expected if the stellar core is both convective and sufficiently large. Figure 11 illustrates the main-sequence evolution of stars with masses of 1.75 and 1.80 $M_{\odot}$ and an initial chemical composition of $(X, Z) = (0.73, 0.01)$. These simulations, performed using MESA v.7184 (Paxton et al. 2011, 2013, 2015), with the same settings as in Saio et al. (2018a); i.e. we employed the Schwarzschild criterion for the convective/radiative boundary, included elemental diffusion to smooth the Brunt-Väisälä frequency, and implemented radiative turbulence to prevent excessive helium settling in the outer envelope. Rotation was not included. The position of HR7495 on the HR diagram is indicated by a black square, with parameters from Table 1. It is evident that HR 7495 is a relatively evolved star, which may still

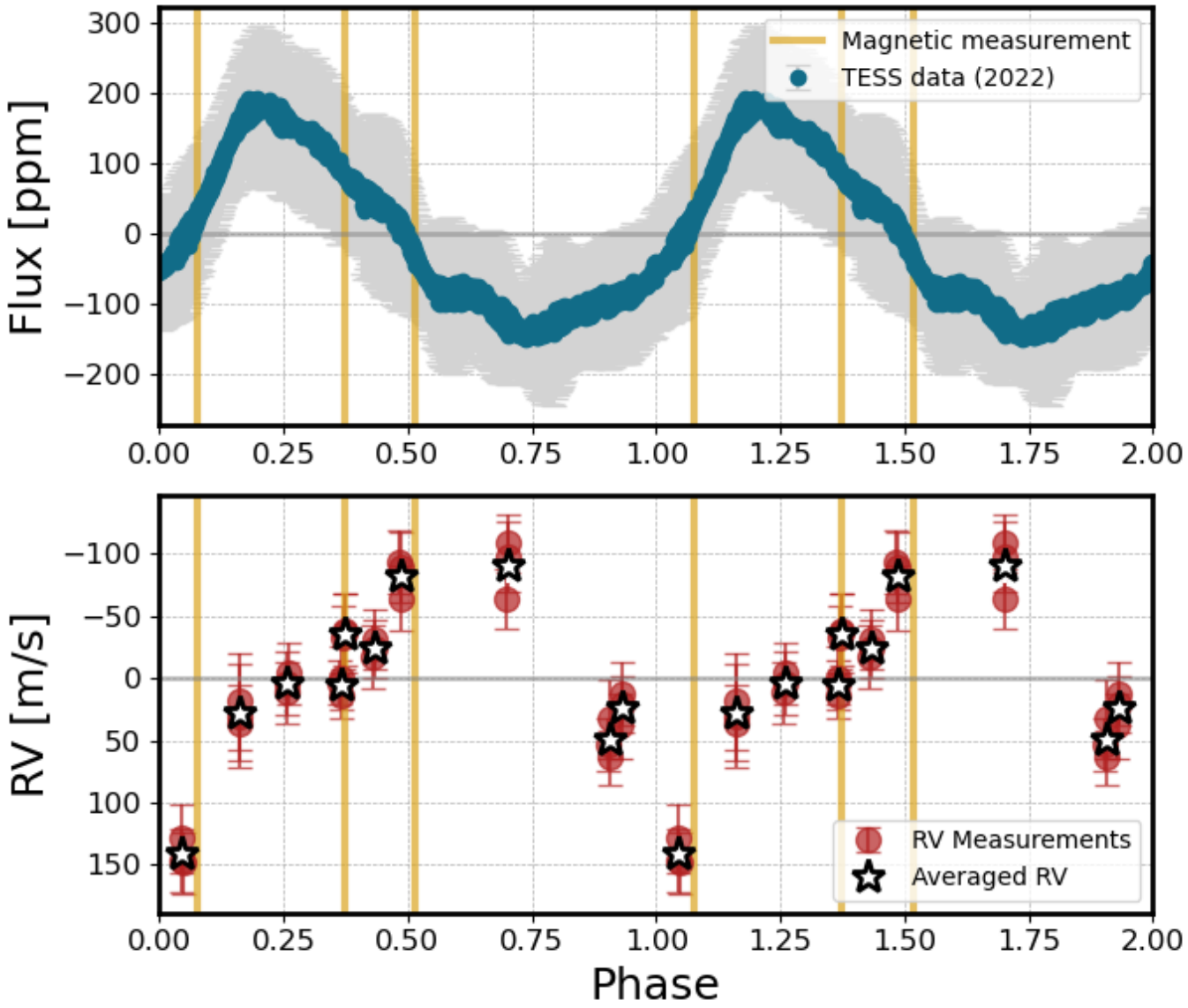

Fig. 10. Upper panel: Phase-folded TESS 2022 data. The data were binned into an arbitrary number of 800 bins, with the gray area indicating the standard deviation within each bin. Lower panel: Phase-folded RV data observed simultaneously with the TESS data. The red data points represent individual observations, while the stars indicate the average value for each bin. Note that the RV measurements for a given epoch are obtained from consecutive spectra (see Table A.1). The vertical yellow lines mark the epochs at which magnetic field measurements were taken, with no significant magnetic field detected.

possess a convective core. Depending on the overshooting parameter, $f_{\rm ov}$, it could be close to the terminal age main sequence (TAMS) or beyond.

Stars with the masses specified above have a small convective core ranging from 0.25 to 0.1$M_{\odot}$ during their main-sequence evolution, as depicted in the right panel of Figure 11. As hydrogen is consumed in the core, the star becomes more luminous and cooler in the HR diagram. The evolutionary track turns abruptly to the left when the hydrogen abundance in the convective core decreases to less than 0.05, at which point the convective core disappears. Therefore, for OsC modes to be excited and explain the observed spikes, the diffusive overshooting parameter, $f_{\rm ov}$, should be greater than 0.2, and the mass M should be at least 1.75$M_{\odot}$, given the adopted initial chemical composition. Since we do not have additional constraints for HR 7495, we cannot conclusively determine which $f_{\rm ov}$ may be appropriate. However, comparing to γ Doradus stars, which have similar masses, Mombarg et al. (2021) showed that stars with masses around 1.80$M_{\odot}$ tend to have a rather large $f_{\rm ov}$, which would suggest that HR 7495 is near the end but still on the main sequence.

7. Conclusions

HR 7495, the brightest 'hump & spike' star known with a visual magnitude of 5.06, is an ideal target to determine whether the spike is of magnetic origin, induced by spots on the stellar surface, or corresponds to OsC modes that propagate to the surface by resonantly exciting g modes. Our target was observed with Kepler for 4.5 years and with TESS during four different seasons. Additionally, we gathered RV measurements contemporaneous with the TESS 2022 data and obtained spectropolarimetric data from three different epochs.

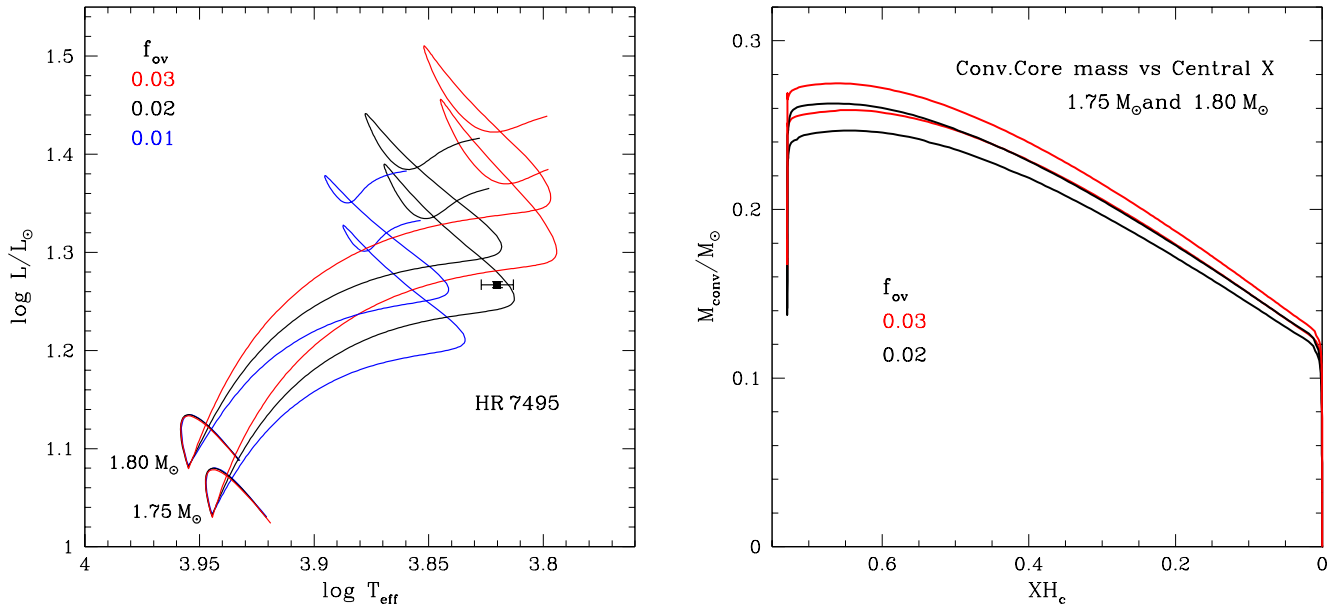

Fig. 11. Left Panel: Evolutionary tracks for masses $M = 1.75, 1.80, M_{\odot}$ with initial chemical composition $(X, Z) = (0.73, 0.01)$. The adopted parameters of diffusive overshooting at the convective core boundary, $f_{\rm ov}$, are color-coded as indicated in the upper left corner. The position of HR 7495 is marked by a filled square with error bars. Right panel: Convective core mass versus central hydrogen abundance X, with $f_{\rm ov}$ color-coded.

Analyzing the shape of the phase-folded light curves, we conclude that they are more consistent with stellar spots, based on their shapes and temporal evolution, which suggests evolving stellar spots. Furthermore, we observed that a subset of the Kepler data shows harmonic peaks of the spike with higher amplitudes than the main spike (Fig. 9), a pattern not expected for OsC modes but indicative of stellar spots.

Our simultaneous 2022 TESS and RV observing campaign shows that the maximum blue shift coincides with the minimum flux (Fig. 10), a phenomenon also observed in the magnetic δ Scuti star HD 188774 (Lampens et al. 2013; Neiner & Lampens 2015). The RV versus flux comparison for HR 7495 suggests that the star has several spots, consistent with the idea of a dynamo-generated magnetic field.

We found no significant magnetic field, which is not unexpected given the low spike amplitude at the epochs of spectropolarimetric measurements (see Table 3) and the evidence for multiple stellar spots. This situation could complicate detection of a significant magnetic field using the LSD method due to potential cancellation effects. Meanwhile, additional high signal-to-noise spectropolarimetric observations of HR 7495 are needed on predicted dates of maximal spike amplitude to check for line profile variability and signatures of magnetic fields.

In the context of OsC modes, we developed a theoretical model to better understand how phase-folded light curves might appear when influenced by m=1, 2, and 3 modes. The model indicated that only significant phase differences between these modes could explain the variability observed in the phase-folded light curves. Our analysis of phase stability and amplitude variations for the three peaks in the Kepler data shows that while the phases remain relatively stable with differences less than $\pi/4$ for two-thirds of the observation period, the amplitudes fluctuate significantly. This observation is consistent with the phase-folded data from Kepler and TESS, as displayed in Figures 5 and 6. Consequently, we conclude that the temporal variability seen in the phase-folded light curves cannot be fully explained by OsC pulsations alone.

While HR 7495 may still be at the end of its main sequence, potentially possessing a convective core large enough to excite OsC modes, the evidence strongly supports a different explanation. The observed spike is consistent with surface rotational modulation induced by stellar spots, suggesting a weak magnetic field. This conclusion is further reinforced by the findings of Henriksen et al. (2023a), which show that 36 out of 162 stars also align with the stellar spots interpretation. Given this comprehensive body of evidence, it is prudent to move beyond the OsC scenario in explaining the spikes observed in all 'hump & spike' stars.

As demonstrated by Henriksen et al. (2023b), there is a discernible correlation between the amplitude of the spike and the power of the Rossby and gravity mode humps, respectively. [6] Our conclusion that the spike is linked to magnetic fields enables further exploration of the role of a subsurface convection zone dynamo and the presence of Rossby and gravity modes. Further, we intend to focus future efforts on characterizing the stellar spots of HR 7495 through additional contemporaneous TESS observations and detailed spectroscopy to analyze line profile variations expected to be observed at the epochs of maximal spike amplitude. Expanding our search in TESS data for more bright 'hump & spike' stars will further our ability to identify ideal candidates for magnetic field measurements using spectropolarimetry.

Acknowledgements. The Center for Computational Astrophysics at the Flatiron Institute is supported by the Simons Foundation. We acknowledge Kepler, TESS, NOT, CFHT, Python, and the use of ChatGPT4 to assist in refining the grammar and helping writing the plotting procedures.

[6] Approximately half of the 'hump & spike' stars exhibit a hump following the spike, indicative of unresolved high-order gravity modes (for more details, see Henriksen et al. 2023b).

References

Balona, L. A. 2017, MNRAS, 467, 1830
Blazère, A., Neiner, C., & Petit, P. 2016, MNRAS, 459, L81
Blazère, A., Petit, P., Neiner, C., et al. 2020, MNRAS, 492, 5794
Buchhave, L. A., Bakos, G. Á., Hartman, J. D., et al. 2010, ApJ, 720, 1118
Cantiello, M. & Braithwaite, J. 2011, A&A, 534, A140
Cantiello, M. & Braithwaite, J. 2019, The Astrophysical Journal, 883, 106
David-Uraz, A., Neiner, C., Sikora, J., et al. 2019, MNRAS, 487, 304
Djupvik, A. A. & Andersen, J. 2010, in Astrophysics and Space Science Proceedings, Vol. 14, Highlights of Spanish Astrophysics V, 211
Donati, J. F., Catala, C., Landstreet, J. D., & Petit, P. 2006, in Astronomical Society of the Pacific Conference Series, Vol. 358, Solar Polarization 4, ed. R. Casini & B. W. Lites, 362
Donati, J. F. & Landstreet, J. D. 2009, ARA&A, 47, 333
Donati, J. F., Semel, M., Carter, B. D., Rees, D. E., & Collier Cameron, A. 1997, MNRAS, 291, 658
Folsom, C. 2024, in preparation
Fuller, J. & Mathis, S. 2023, MNRAS, 520, 5573
Gaia Collaboration, Vallenari, A., Brown, A. G. A., et al. 2022, Gaia Data Release 3: Summary of the content and survey properties
Henriksen, A. I., Antoci, V., Saio, H., et al. 2023a, MNRAS, 520, 216
Henriksen, A. I., Antoci, V., Saio, H., et al. 2023b, MNRAS, 524, 4196
Jeffers, S. V., Kiefer, R., & Metcalfe, T. S. 2023, Space Sci. Rev., 219, 54
Koch, D. G., Borucki, W. J., Basri, G., et al. 2010, ApJ, 713, L79
Kolodziejczak, J. & Caldwell, D. 2011, Science from Kepler Collateral Data: 150 ksec/year from 13 Million Stars?, Tech. Rep. 20120003045, NASA Marshall Space Flight Centre
Lallement, R., Babusiaux, C., Vergely, J. L., et al. 2019, A&A, 625, A135
Lampens, P., Tkachenko, A., Lehmann, H., et al. 2013, A&A, 549, A104
Lee, U. 2021, Monthly Notices of the Royal Astronomical Society, 505, 1495
Lee, U. & Saio, H. 1997, ApJ, 491, 839
Lee, U. & Saio, H. 2020, Monthly Notices of the Royal Astronomical Society, 497, 4117
Lenz, P. & Breger, M. 2014, Period04: Statistical analysis of large astronomical time series, Astrophysics Source Code Library, record ascl:1407.009
Lignières, F., Petit, P., Böhm, T., & Aurière, M. 2009, A&A, 500, L41
Mombarg, J. S. G., Van Reeth, T., & Aerts, C. 2021, A&A, 650, A58
Neiner, C. & Lampens, P. 2015, MNRAS, 454, L86
Neiner, C., Wade, G. A., & Sikora, J. 2017, MNRAS, 468, L46
Paxton, B., Bildsten, L., Dotter, A., et al. 2011, ApJS, 192, 3
Paxton, B., Cantiello, M., Arras, P., et al. 2013, ApJS, 208, 4
Paxton, B., Marchant, P., Schwab, J., et al. 2015, ApJS, 220, 15
Petit, P., Lignières, F., Aurière, M., et al. 2011, A&A, 532, L13
Pope, B. J. S., Davies, G. R., Hawkins, K., et al. 2019, ApJS, 244, 18
Pope, B. J. S., White, T. R., Huber, D., et al. 2016, MNRAS, 455, L36
Ricker, G. R., Winn, J. N., Vanderspek, R., et al. 2015, JATIS, 1
Saio, H., Bedding, T. R., Kurtz, D. W., et al. 2018a, MNRAS, 477, 2183
Saio, H., Kurtz, D. W., Murphy, S. J., Antoci, V. L., & Lee, U. 2018b, MNRAS, 474, 2774
Sikora, J., Wade, G. A., & Rowe, J. 2020, MNRAS, 498, 2456
Telting, J. H., Avila, G., Buchhave, L., et al. 2014, Astronomische Nachrichten, 335, 41
Thomson-Paressant, K., Neiner, C., Lampens, P., et al. 2023, MNRAS, 526, 1728
Townsend, R. H. D. 2003, MNRAS, 340, 1020
Trust, O., Jurua, E., De Cat, P., & Joshi, S. 2020, MNRAS, 492, 3143
Zwintz, Neiner, C., Kochukhov, O., et al. 2020, A&A, 643, A110

Appendix A: Radial velocity measurements with FIES.

Table A.1. Radial Velocity Observations of HR 7459. The SNR is the averaged signal-to-noise ratio computed from the red and the blue part of the spectrum. The spectrum highlighted with the asterisk is the template we used to extract the RV measuremnts.

BJD	RV [ms^{-1}]	RV$_{err}$ [ms^{-1}]	SNR
2459767.4210620	53.16	21.43	155
2459767.4225670	32.62	31.51	147
2459767.4240100	63.86	22.28	149
2459772.5318530	4.02	17.61	186
2459772.5333270	14.31	18.03	208
*2459772.5348040	0	25.37	211
2459777.4590920	-63.82	24.07	189
2459777.4605710	-97.47	28.58	188
2459777.4620350	-108.35	23.49	188
2459787.4792280	-92.8	25.26	154
2459787.4807010	-63.93	26.01	160
2459787.4821640	-89.03	28.32	168
2459791.5759690	11.8	24.57	154
2459791.5774470	4.27	25.09	146
2459791.5789000	-3.81	24.43	134
2459798.4758930	38.57	25.54	180
2459798.4773910	21.07	23.01	170
2459798.4788420	12.49	25.57	177
2459800.6054390	-32.51	25.39	183
2459800.6069090	-38.52	28.63	186
2459800.6083960	-36.21	31.47	188
2459807.5096020	146.55	24.99	163
2459807.5111030	128.82	27.92	173
2459807.5125530	148.38	24.77	170
2459813.5872670	18.78	38.7	75
2459813.5887580	36.01	30.54	95
2459813.5902660	30.53	41.61	109
2459818.4188420	-16.76	25.19	164
2459818.4203100	-31.57	23.92	171
2459818.4217870	-23.55	23.13	160